Journal of Quantitative Spectroscopy & Radiative Transfer 148 (2014) 156–164

Contents lists available at ScienceDirect

Journal of Quantitative Spectroscopy & Radiative Transfer

journal homepage: www.elsevier.com/locate/jqsrt

Consideration of enhancement of thermal rectification using metamaterial models

Hideo Iizuka [a,*], Shanhui Fan [b,*]

[a] Toyota Central Research & Development Labs., Nagakute, Aichi 480 1192, Japan
[b] Department of Electrical Engineering, Stanford University, Stanford, CA 94305, USA

ARTICLE INFO

Article history:
Received 24 April 2014
Received in revised form
12 June 2014
Accepted 8 July 2014
Available online 17 July 2014

Keywords:
Heat transfer
Near-field
Metamaterials
Radiative
Thermal rectification

ABSTRACT

We present a systematic study to highlight some of the fundamental physics that governs metamaterial based electromagnetic thermal rectifiers. In such thermal rectifiers, the rectification arises from the alignment or misalignment of surface resonances in the forward or reverse scenarios, whereas the bulk states of metamaterials do not contribute to rectification. Therefore, we show that one can understand the behavior of such rectifiers by examining the relative excitation strength of the surface and bulk resonances. We verify such an understanding by accounting for the dependence of the contrast ratio on various parameters that define the dielectric response of the metamaterials.

1. Introduction

Manipulating heat flow at nanoscale has generated substantial interests for thermal management of electronic and optical devices and energy systems [1]. A key technique for manipulating nanoscale heat transfer is through the use of near-field electromagnetic heat transfer. Electromagnetic heat transfer in the near-field regime exceeds the far-field blackbody limit due to coupling between thermally excited surface resonances [2,3]. Significant theoretical [4–13] and experimental [14–19] progresses have been made in the past decade in this research area, and potential applications are now emerging [20–26].

These recent progresses have pointed to the importance of the capability for designing and controlling the properties of near-field thermal transfer. Thus, while earlier studies of near-field thermal transfer typically assumed the use of naturally existing materials, there are now interests in exploring the use of metamaterials for additional flexibility in designing the properties of near-field thermal transfer [27–32]. Similarly, while earlier studies focused on near-field thermal transfer primarily as a passive process, there are now significant efforts in developing active control of near-field thermal transfer. In particular, thermal rectification schemes in electromagnetic heat transfer have been extensively studied [33–40] since its initial proposal five years ago [33].

In Ref. [33], the rectification arises from the alignment or misalignment of surface resonances in the forward or backward temperature biased scenarios, respectively. The concept in Ref. [33] has been implemented numerically assuming a variety of naturally occuring materials, including various polytypes of SiC [33,34], SiO_2 [35], heavily doped silicon [36], and phase-changed materials [37–39]. The performances of the rectifiers in each of these cases are dictated by the resonant properties of these materials. On the other hand, with the development of metamaterials, one should be able to, at least in principle, control the resonant properties. Therefore, it is important to understand how various resonant properties, in general, influence the performance of a thermal rectifier.

* Corresponding authors.
E-mail addresses: hiizuka@mosk.tytlabs.co.jp (H. Iizuka), shanhui@stanford.edu (S. Fan).

http://dx.doi.org/10.1016/j.jqsrt.2014.07.007
0022-4073/

In this paper, we present a systematic study to highlight some of the fundamental physics that governs metamaterial-based electromagnetic thermal rectifiers, where two metamaterial planar bodies are brought in close proximity. Thermal transfer is determined by the permittivity and the permeability of the materials. The use of metamaterials enables one to achieve permittivity and/or permeability in a range of positive, zero, or negative values. In this paper, we consider a material described by the Drude model; such a model can be achieved either with metamaterials [41,42] or with heavily doped semiconductors [4,5]. We show that one can understand the behavior of such rectifiers by examining the relative excitation strength of the surface and bulk resonances.

This paper is organized as follows. In Section 2, a model system of electromagnetic thermal rectifier is presented. In Section 3, we introduce an analytic theory for maximizing thermal rectification. In Section 4, we present numerical results and illustrate how the thermal rectification phenomenon is controlled by various parameters that define the dielectric response of the metamaterials, by accounting for the dependence of the contrast ratio of the surface state to the bulk state excitations on these parameters. The paper is then concluded in Section 5.

2. Model system

We consider a metamaterial with its permittivity described by a Drude model:

$$\varepsilon_d(\omega)=\varepsilon_\infty-\frac{{\omega_p}^2}{\omega(\omega+ig_m)}, \tag{1}$$

ε_∞, ω_p, g_m, and ω are the permittivity at infinite frequency, the plasma frequency, the damping constant, and the frequency, respectively. We assume an $\exp(-i\omega t)$ convention throughout the paper. With metamaterial design, one should be able to control both ε_∞ and ω_p in Eq. (1) [42]. Therefore, the goal of our study is to elucidate how the material parameters in Eq. (1) influence the behavior of a thermal rectifier.

We will see that such an influence can be understood in terms of the dependency of various resonant properties on the material parameters. Thus we first briefly review the relevant resonances. In the lossless case, with $g_m=0$, the material supports a bulk plasmon resonance occuring at $\varepsilon_d(\omega_{bp})=0$ with $\omega_{bp}=\omega_p/\sqrt{\varepsilon_\infty}$. In addition, an interface between such metamaterial and vacuum supports a surface plasmon resonance occuring at $\varepsilon_d(\omega_{sp})=-1$ with $\omega_{sp}=\omega_p/\sqrt{\varepsilon_\infty+1}$.

Using such a metamaterial model we consider an electromagnetic thermal rectification system, as shown in Fig. 1(a). It consists of two semi-infinite metamaterial plates separated by a vacuum gap. The vacuum gap, the bottom and the top plates are labeled as 0, 1, and 2, respectively. The two metamaterial plates are maintained at different temperatures T_H and T_L ($T_H>T_L$). Since $T_H\neq T_L$, the system is in a nonequilibrium condition. We assume that both plates are described by the Drude model of Eq. (1). To achieve thermal rectification, the dielectric properties of the metamaterial must be temperature dependent [33–40]. In the forward biased scenario (left panel, Fig. 1a), with plate 1 at temperature T_H and plate 2 at T_L, we assume that both metamaterial plates have the same permittivity $\varepsilon_d(\omega)$, hence the surface resonances at the two material-vacuum interfaces have the same frequencies, whereas in the reverse biased scenario where we reverse the temperature bias (right panel, Fig. 1a), we assume that the two metamaterials have their dielectric functions described by

$$\varepsilon_{d,\,\pm\Delta\omega_p}(\omega)=\varepsilon_\infty-\frac{(\omega_p\pm\Delta\omega_p)^2}{\omega(\omega+ig_m)}. \tag{2}$$

In the reverse biased case the surface resonances at the two interfaces differ by a frequency $2\Delta\omega_{sp}=2\Delta\omega_p/\sqrt{\varepsilon_\infty+1}$.

The heat transfer between the plates is calculated using the framework of the fluctuational electrodynamics. The electric and magnetic fields are calculated by integrating contributions from the thermal current sources whose strengths are provided by the fluctuation dissipation theorem, and by using the dyadic Green's functions of the system. Then the ensemble average of Poynting vector, represented as a cross correlation function of the electric and magnetic fields, is determined [2]. The cylindrical coordinate system (R, ϕ, z) is used in the computation. Using the formalism described above, the net heat flux ϕ_F for the forward scenario is given by [4]

$$\phi_F=\int_0^{+\infty}d\omega[\Theta(\omega,T_H)-\Theta(\omega,T_L)]\times\int_0^{+\infty}Z(\omega,\beta,\varepsilon_1=\varepsilon_d(\omega),\varepsilon_2=\varepsilon_d(\omega))\beta d\beta, \tag{3a}$$

where the exchange function

$$\int_0^{+\infty}Z(\omega,\beta,\varepsilon_1,\varepsilon_2)\beta d\beta=\sum_{j=s,p}\left[\int_0^{k_0}\frac{(1-|r_{01,j}|^2)(1-|r_{02,j}|^2)}{4\pi^2|1-r_{01,j}r_{02,j}e^{2i\gamma_0 d}|^2}\beta d\beta+\int_{k_0}^{+\infty}\frac{Im(r_{01,j})Im(r_{02,j})e^{-2Im(\gamma_0)d}}{\pi^2|1-r_{01,j}r_{02,j}e^{-2Im(\gamma_0)d}|^2}\beta d\beta\right], \tag{3b}$$

$\Theta(\omega,T)=\hbar\omega/(e^{\hbar\omega/(k_BT)}-1)$ is the mean thermal energy of a single optical mode at a frequency ω. $\hbar$ and k_B are the reduced Planck constant and the Boltzmann constant, respectively. $r_{uv,\,j}$ is the Fresnel reflection coefficient from media u to v and the subscripts $j=s,p$ represent the two polarizations. γ_0 is the z-component of the free space wavevector $\boldsymbol{k_0}$ ($k_0=|\boldsymbol{k_0}|$) and has the form $\gamma_0=\sqrt{{k_0}^2-\beta^2}$, ($\beta<k_0$) for propagating waves and $\gamma_0=i\sqrt{\beta^2-{k_0}^2}$ ($k_0<\beta$) for evanescent waves. β is the radial-component of $\boldsymbol{k_0}$. Eq. (3b) includes the contributions of both propagating and evanescent waves. Similar to the forward scenario, the net heat flux ϕ_R for the reverse scenario is calculated with the exchange function $Z(\omega,\beta,\varepsilon_1=\varepsilon_{d,+\Delta\omega_p}(\omega),\ \varepsilon_2=\varepsilon_{d,-\Delta\omega_p}(\omega))$.

3. Theoretical consideration for maximizing the contrast ratio in thermal rectifier

As a typical example of a thermal rectifier, we consider the system shown in Fig. 1, with a parameter set described

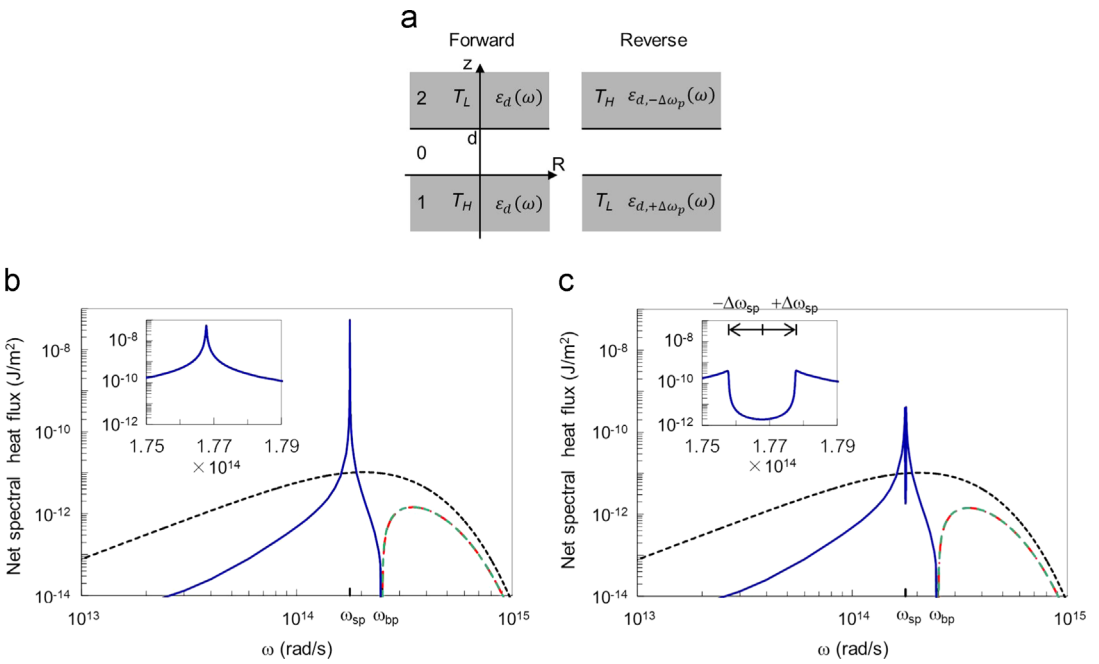

Fig. 1. (a) A thermal rectification system using metamaterials. In the forward temperature biased scenario (left panel), the semi-infinite bottom and top plates have the same permittivity $\varepsilon_d(\omega)$ as described by Eq. (1), whereas in the reverse temperature biased scenario (right panel), each plate has slightly different permittivities $\varepsilon_{d,+\Delta\omega_p}(\omega)$ and $\varepsilon_{d,-\Delta\omega_p}(\omega)$ in Eq. (2). Spectra of net heat flux are shown in (b) for the forward scenario and in (c) for the reverse scenario. The insets show enlarged spectra around the surface resonance ω_{sp}. (blue solid lines: evanescent p-polarization, green dashed lines: propagation p-polarization, red dashed-dotted lines: propagation s-polarization, the evanescent s-polarization is negligibly small.) Blackbody radiation (black dotted lines) is plotted as a reference. Parameters are $d=100$ nm, $T_H=500$ K, $T_L=300$ K, $\Delta\omega_p=1.4\times10^{12}$ rad/s, $\varepsilon_\infty=1$, $\omega_p=2.5\times10^{14}$ rad/s, and $g_m=1.7\times10^{10}$ rad/s. These values are used for other calculations unless mentioned. (For interpretation of the references to color in this figure legend, the reader is referred to the web version of this article.)

in details in the captions of Fig. 1(b) and (c). We choose a distance between the plates, $d=100$ nm, and temperatures $T_H=500$ K, $T_L=300$ K, based on recent experimental investigations [14–19]. We assume a plasma frequency $\omega_p=2.5\times10^{14}$ rad/s and a plasma frequency shift $\Delta\omega_p=1.4\times10^{12}$ rad/s. These values are similar to those of the thermal rectifier based on silicon carbide [33,34]. The amount of $\Delta\omega_{sp}$ is generally limited by the material properties, and the value used here approximately corresponds to that of silicon carbide. With the parameters above fixed, the system in Fig. 1 corresponds to the optimal case in terms of the rectification contrast ratio as we vary the permittivity at infinite frequency ε_∞ and the damping constant g_m. Such optimal case has $\varepsilon_\infty=1$ and $g_m=1.7\times10^{10}$ rad/s.

For this optimal case, we see a single strong peak of heat transfer via the p-polarized evanescent wave at the surface resonance frequency ω_{sp} in the forward biased scenario (blue solid line in Fig. 1b). In this scenario, since the two metamaterial plates have the same plasma frequency, the two metamaterial/vacuum interfaces support surface plasmon at the same frequency. In contrast, in the reverse biased scenario, the plasma frequencies of the two metamaterials differ by $2\Delta\omega_p$. The surface plasmon resonances for the two interfaces thus differ by $2\Delta\omega_{sp}$. The misalignment of the surface resonances at the two interfaces results in two peaks in the thermal transfer spectrum, and greatly reduced thermal transfer (blue solid line in Fig. 1c). The thermal rectification in this system therefore arises from thermal excitation of the surface states, in consistency with near-field thermal rectifiers in Refs. [33–38]. The surface state contribution is dominated by the p-polarization with contributions from the s-polarization being almost negligible.

In addition to contributions from surface excitation, part of the thermal transfer between the two plates comes from the excitations of the bulk states in each plate. In the spectra shown in Fig. 1(b) and (c), the contributions from the bulk states correspond to spectral components above ω_{bp}; $\omega_p/\sqrt{\varepsilon_\infty}$ for both plates in the forward scenario and $(\omega_p\pm\Delta\omega_p)/\sqrt{\varepsilon_\infty}$ for the two plates, respectively, for the reverse scenario. The bulk contribution has significant components in both p- and s-polarized propagation waves. Comparing Fig. 1(b) and (c), we see that there is almost no difference in the heat flux spectra in both the forward and reverse scenarios for the contributions from the bulk states. As a side note, at the bulk resonance, the thermal transfer is very small but not zero as seen in Fig. 1(b) and (c).

Based on the spectra presented above, we show quantitatively that the contrast ratio in thermal rectification can be understood in terms of the relative excitation strength between the bulk and the surface states. Thermal rectification contrast ratio can be written as

$$R_T=\frac{\phi_F-\phi_R}{\phi_R}=\frac{(\phi_{F,S}+\phi_{F,B})-(\phi_{R,S}+\phi_{R,B})}{\phi_{R,S}+\phi_{R,B}}, \tag{4}$$

where each net heat flux is expressed as a sum of the contributions of the surface state and the bulk state, as denoted by the subscripts, S and B, respectively. Assuming

$\phi_{F,B} \approx \phi_{R,B} \approx \phi_B$ as observed from Fig. 1(b) and (c), the thermal rectification contrast ratio of Eq. (4) is then simplified to

$$R_T \approx \frac{\phi_{F,S}-\phi_{R,S}}{\phi_{R,S}} \frac{\phi_{R,S}}{\phi_{R,S}+\phi_B} = S^0 \eta, \tag{5}$$

where the 1st term S^0 represents the contrast ratio between the forward and the reverse scenarios of the surface state contribution. The 2nd term η represents the fraction of the surface state contribution in the total net heat transfer of the reverse scenario and is given by

$$\eta \approx \frac{\int_0^{+\infty} d\omega[\Theta(\omega,T_H)-\Theta(\omega,T_L)] \int_{k_0}^{+\infty} \frac{Im(r_{01,p})Im(r_{02,p})e^{-2Im(\gamma_0)d}}{\pi^2|1-r_{01,p}r_{02,p}e^{-2Im(\gamma_0)d}|^2}\beta \, d\beta}{\int_0^{+\infty} d\omega[\Theta(\omega,T_H)-\Theta(\omega,T_L)] \left[\int_{k_0}^{+\infty} \frac{Im(r_{01,p})Im(r_{02,p})e^{-2Im(\gamma_0)d}}{\pi^2|1-r_{01,p}r_{02,p}e^{-2Im(\gamma_0)d}|^2}\beta d\beta + \sum_{j=s,p} \int_0^{k_0} \frac{(1-|r_{01,j}|^2)(1-|r_{02,j}|^2)}{4\pi^2|1-r_{01,j}r_{02,j}e^{2i\gamma_0 d}|^2}\beta \, d\beta\right]}, \tag{6}$$

where the Fresnel reflection coefficients in Eq. (6) are obtained in the reverse scenario. A key to maximizing the rectification contrast ratio is therefore to maximize the fraction η of the surface state contribution.

In Eq. (5), the contrast ratio S^0 of the surface state contribution in the forward and reverse scenarios can be understood using the coupled mode theory formalism. The coupled mode theory provides a general description of any resonance phenomenon in terms of how resonant modes are coupled and how energy decays in each mode [43]. In Ref. [44], a quantum mechanical description of the heat transfer dynamics for two plasmonic nanoparticles was presented. Here we consider a single-channel heat transfer by the coupled mode theory and clarify the coupling phenomenon of the dominant modes and the relationship of the dielectric response to thermal rectification. As seen in Eq. (3), the net heat flux is described by a collection of independent thermal energy transfer channels indexed by the radial wavenumber β. The thermal transfer in a single channel can be described using the two-mode coupled mode theory [33]

$$\frac{da_1}{dt} = -i\omega_1 a_1 - \gamma_1 a_1 - i\kappa_{12} a_2 + \sqrt{2\gamma_1} n_1, \tag{7a}$$

$$\frac{da_2}{dt} = -i\omega_2 a_2 - \gamma_2 a_2 - i\kappa_{21} a_1 + \sqrt{2\gamma_2} n_2, \tag{7b}$$

where ω_1 and ω_2 are the resonance frequencies, γ_1 and γ_2 are the loss rates, n_1 and n_2 are the noise sources for metamaterial plates 1 and 2. κ_{12} and κ_{21} are the coupling rates between the two modes and the energy conservation constrains $k_{12} = k_{21}^*$. The correlations of the noise sources are given by

$$\langle n_1(\omega) n_1^*(\omega') \rangle = \Theta(\omega, T_1) 2\pi\delta(\omega-\omega'), \tag{8a}$$

$$\langle n_2(\omega) n_2^*(\omega') \rangle = \Theta(\omega, T_2) 2\pi\delta(\omega-\omega'), \tag{8b}$$

$$\langle n_1(\omega) n_2^*(\omega') \rangle = \langle n_2(\omega) n_1^*(\omega') \rangle = 0. \tag{8c}$$

We normalize the mode amplitudes a_1 and a_2, so that the mode energies are given by $|a_1|^2$ and $|a_2|^2$. Following [33], for a single channel the power transfer for the forward and reverse scenarios in our system is

$$S(t) = \int_{-\infty}^{+\infty} d\omega \langle S(\omega) \rangle = \int_{-\infty}^{+\infty} d\omega \frac{2\kappa^2 \gamma_1 \gamma_2}{\pi} \frac{\Theta(\omega,T_H)-\Theta(\omega,T_L)}{|\{i[\omega-(\omega_{sp}+\Delta\omega)]+\gamma_1\}\{i[\omega-(\omega_{sp}-\Delta\omega)]+\gamma_2\}+\kappa^2|^2}, \tag{9}$$

where $|k|^2 = k_{12}k_{21}^*$ and we have assumed that the modes at the two plates for this channel have frequencies $\omega_{sp}+\Delta\omega$ and $\omega_{sp}-\Delta\omega$, respectively.

In our system, the gap size is at the deep sub-wavelength scale. The modes that are relevant for near-field thermal transfer also have a spatial dimension that is at deep sub-wavelength scale. For these modes, it is known that their intrinsic decay rate is pinned at half of the damping rate in the Drude model [45–47]. Therefore, we can replace the damping rate γ_1 and γ_2 in Eq. (9) with the same $\gamma = g_m/2$.

Eq. (9) describes the thermal transfer in a single β channel of surface-state contributions in the forward and reverse bias scenarios, where the resonant frequency of the channel is close to the corresponding surface plasmon frequencies in the two scenarios. To compute the total thermal transfer, one needs to integrate over β in the same fashion as in Eqs. (3a) and (3b). However, for both the forward and backward scenarios, in our system the integrand in such a β integral is typically sharply peaked at a single β value. As a result, we can use Eq. (9) to account for the *total* thermal transfer in the forward and backward scenarios. We note in arriving at this result, we do not assume that the integrands in the forward and backward scenarios peak at the same beta value, as long as we use Eq. (9) to describe the channels that are dominant in the forward and backward bias scenarios, respectively. In our

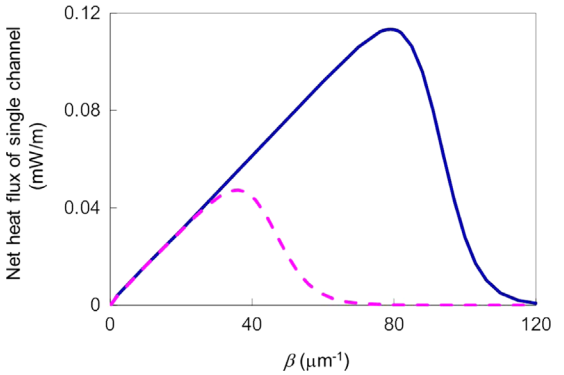

Fig. 2. Net heat flux of a single channel as a function of the wavenumber β (blue solid line: forward scenario, pink dashed line: reverse scenario). (For interpretation of the references to color in this figure legend, the reader is referred to the web version of this article.)

system, the dominant channels in the two scenarios in fact have different β values. As shown in Fig. 2, the dominant channel with a parameter set in the caption of Fig. 1 has a lateral wavenumber $\beta_F = 79\ \mu m^{-1}$ for the forward scenario and $\beta_R = 36\ \mu m^{-1}$ for the reverse scenario that are obtained using the integrand of Eq. (3). For the reverse scenario, the dominant channel has a larger difference in the resonant frequencies, $2\Delta\omega = 4.86 \times 10^{12}$ rad/s in Eq. (9), as compared to the frequency difference of surface resonances for the thermal transfer, $2\Delta\omega_{sp}$.

Since the spectral response of power transfer in our system is sharply peaked around ω_{sp} in both the forward and reverse scenarios, we approximately move $\Theta(\omega, T)$ out of the integration as $\Theta(\omega_{sp}, T)$ and analytically evaluate the integral in Eq. (9)

$$\begin{aligned}\langle S(t)\rangle &\approx \left[\Theta(\omega_{sp}, T_H) - \Theta(\omega_{sp}, T_L)\right] \times \int_{-\infty}^{+\infty} d\omega \frac{2\kappa^2\gamma^2}{\pi} \frac{1}{|\{i[\omega-(\omega_{sp}-\Delta\omega)]+\gamma\}\{i[\omega-(\omega_{sp}+\Delta\omega)]+\gamma\}+\kappa^2|^2} \\ &= \left[\Theta(\omega_{sp}, T_H) - \Theta(\omega_{sp}, T_L)\right] \frac{\kappa^2\gamma}{(\Delta\omega)^2+\kappa^2+\gamma^2}. \end{aligned} \tag{10}$$

In obtaining the final result in Eq. (10), we have used the contour integral method. Among the four poles, two of them $\omega = \omega_{sp} \pm \sqrt{(\Delta\omega)^2+\kappa^2} + i\gamma$ are located in the upper half of the complex plane and contribute to the integral. Substituting Eq. (10) multiplied by β into Eq. (4), the rectification contrast ratio of the dominant single channels is given by

$$R_{T,\beta} = \frac{\beta_F \kappa_F{}^2[(\Delta\omega_R)^2+\kappa_R{}^2+\gamma^2] - \beta_R \kappa_R{}^2[(\Delta\omega_F)^2+\kappa_F{}^2+\gamma^2]}{\beta_R \kappa_R{}^2[(\Delta\omega_F)^2+\kappa_F{}^2+\gamma^2]}, \tag{11}$$

where subscripts F and R represent the forward and reverse scenarios. $2\Delta\omega_F$ and $2\Delta\omega_R$ denote the differences of the two resonant frequencies at the dominant channels in the forward and reverse scenarios, respectively. Note that frequency differences at a single channel become larger with the decrease of the wavenumber of the channel due to stronger coupling between the two surfaces as wavenumber decreases. We clearly see in Eq. (11) that the rectification contrast ratio for the surface state is independent of ω_p. Moreover, Eq. (11) indicates that large shift $\Delta\omega_R$, which is attributed to large shift $\Delta\omega_{sp}$ in surface resonance frequencies and small wavenumber β_R of the reverse scenario, enhances thermal rectification. The increase in the loss rate γ reduces thermal rectification, as seen in Eq. (11).

Certainly all numerical results can be obtained with Eq. (3). The coupled mode theory results in a greatly simplified closed-form formula for rectification (Eq. (11)), where each parameter has a clear physical meaning. Use of the coupled mode theory therefore serves the purpose of elucidating the underlying physics.

We compare the net spectral heat flux of a single channel obtained by the fluctuational electrodynamics calculation and by the coupled mode theory in Fig. 3. We consider the dominant channel for each scenario. In the forward bias scenario, the resonant frequency in this channel is very close to ω_{sp}. For the fluctuational electrodynamics calculation we used the integrand of Eq. (3), whereas for the coupled mode theory calculation we used Eq. (9) with parameters in the caption of Fig. 3. The two calculations showed excellent agreement. Therefore, one can use the coupled mode theory model, which is far simpler, to understand the thermal rectification behavior of this system.

Both the bulk and the surface states contribute to thermal transfer. However, the contrast in the forward and backward scenarios, which is essential for achieving thermal rectification, is only present in the surface state contribution. Therefore, the thermal rectification contrast ratio R_T may be enhanced by maximizing the contribution of the surface states, while minimizing the excitation of the bulk state [i.e., trying to reach $\eta \approx 1$ in Eq. (5)]. In addition, further enhancement of the thermal rectification contrast ratio can be

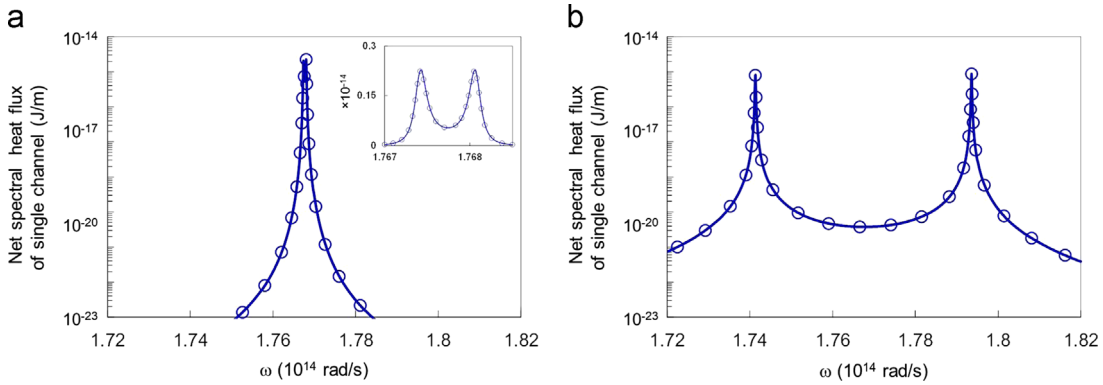

Fig. 3. Spectra of net heat flux of a single channel for (a) the forward scenario at $\beta_F = 79\ \mu m^{-1}$ and for (b) the reverse scenario at $\beta_R = 36\ \mu m^{-1}$. The curves represent the spectra of net heat flux obtained using the fluctuational electrodynamics. The fitting symbols are obtained by the coupled mode theory with a coupling rate of $\kappa_F = 1.3 \times 10^{10}$ rad/s, a frequency shift of $\Delta\omega_F = 3 \times 10^{10}$ rad/s, and a loss rate of $\gamma_1 = \gamma_2 = g_m/2 = 8.5 \times 10^9$ rad/s for the forward scenario and $\kappa_R = 9.6 \times 10^{11}$ rad/s, $\Delta\omega_R = 2.43 \times 10^{12}$ rad/s, and $\gamma_1 = \gamma_2 = g_m/2 = 8.5 \times 10^9$ rad/s for the reverse scenario in Eq. (9). The inset shows the enlarged spectrum in a linear scale around resonance ω_{sp}.

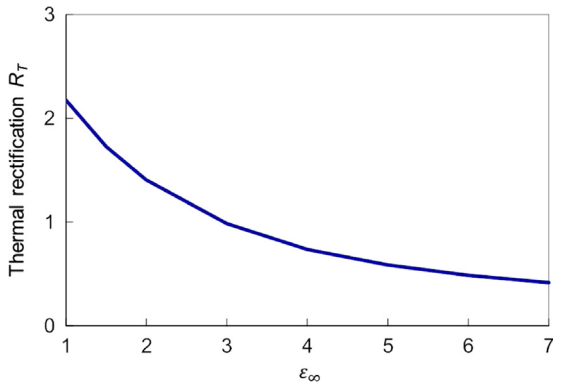

Fig. 4. Thermal rectification as a function of the permittivity at infinite frequency, ε_∞.

achieved by enhancing the contrast ratio in surface state contribution, i.e., by maximizing S^0. Such understanding is crucial for the discussion in the next section.

4. Results

Based on the above understanding regarding the different roles that bulk and surface states excitations play in thermal rectification, in this section we explore the dependence of the contrast ratio in our thermal rectification system, particularly on three parameters that define the dielectric response of the metamaterials: permittivity ε_∞ at infinite frequency, damping constant g_m, and plasma frequency ω_p in Eq. (1). In each of the studies below, unless otherwise mentioned, we start with the parameters as shown in Fig. 1, and vary only one parameter while keeping all other parameters fixed.

4.1. Dependency of contrast ratio on ε_∞

We first consider the dependence of a parameter of ε_∞ on thermal rectification. Fig. 4 shows the thermal rectification contrast ratio as a function of ε_∞. Rectification coefficient maximizes at $\varepsilon_\infty=1$ and decreases with the increase of ε_∞.

The dependency of the contrast ratio on ε_∞ in Fig. 4 can be understood from the dispersion relations of the metamaterial/vacuum interface as plotted in Fig. 5, where we consider two cases: $\varepsilon_\infty=1$ in Fig. 5(a) and $\varepsilon_\infty=5$ in Fig. 5 (b). For each case, the dispersion relations include both the surface states and the bulk states. The dispersion relation of the surface state is described by

$$\beta=(\omega/c)\sqrt{\varepsilon_d/(\varepsilon_d+1)}, \tag{12}$$

where c is the speed of light. The bulk state forms a continuum above frequency ω_{bp}. In Fig. 5, we see that the frequency difference between the surface state resonance ω_{sp} and the bulk state resonance ω_{bp}, which is the band edge frequency of extended modes in the metamaterial, is maximized for $\varepsilon_\infty=1$ (Fig. 5a). Therefore, from the discussion on Eq. (5) we expect that the thermal rectification is maximized at $\varepsilon_\infty=1$. Increasing ε_∞ reduces the frequency separation between the surface and bulk states, and leads

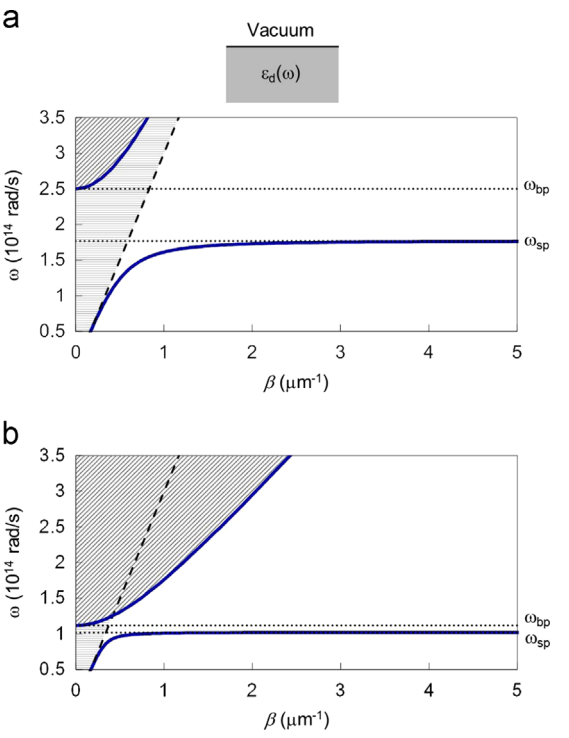

Fig. 5. Dispersion curves (blue solid lines) of the lossless metamaterial/vacuum interface for different permittivities at infinite frequency: (a) $\varepsilon_\infty=1$ and (b) $\varepsilon_\infty=5$. The shaded areas with oblique lines and horizontal lines represent continuum modes that are extended in metamaterial and in vacuum, respectively. The light line is represented by the black dashed line. (For interpretation of the references to color in this figure legend, the reader is referred to the web version of this article.)

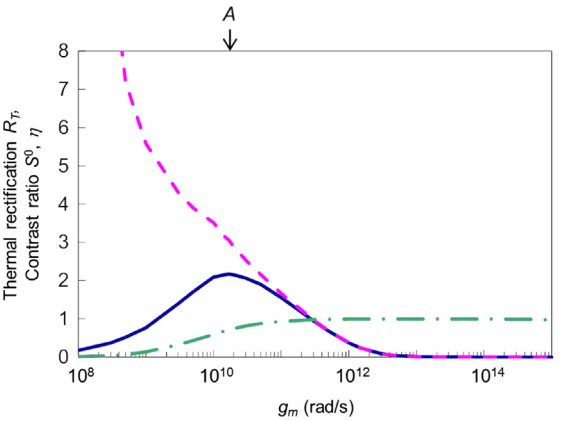

Fig. 6. Thermal rectification (blue solid line) as a function of the damping constant g_m. The contrast ratios of the surface state contribution of the forward to the reverse scenarios (S^0 in Eq. (5), pink dashed line) and the surface state contribution to the total heat transfer (η in Eqs. (5) and (6), green dashed-dotted line) are presented. Label A indicates the g_m value for the spectra of Fig. 1(a) and (b). (For interpretation of the references to color in this figure legend, the reader is referred to the web version of this article.)

to the reduction of the thermal rectification contrast ratio as shown in Fig. 4. This result confirms that thermal rectification is maximized when the surface state resonance

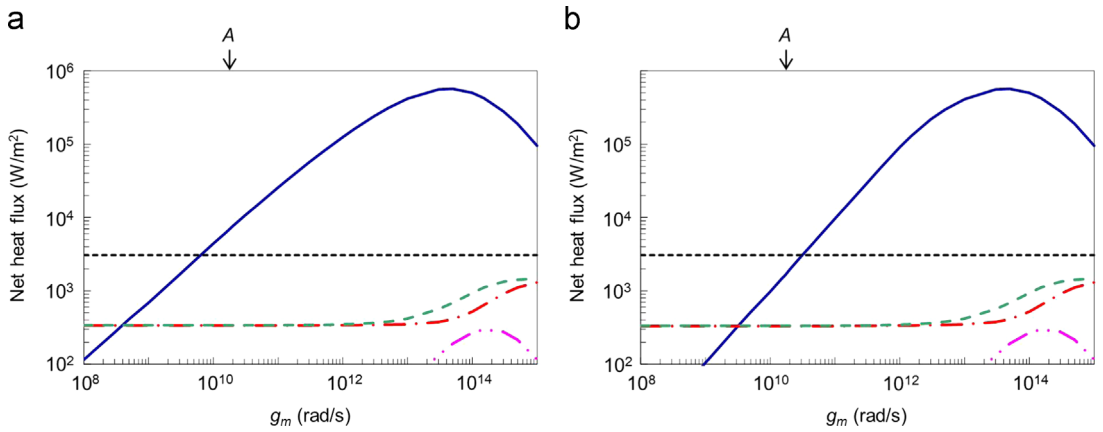

Fig. 7. Net heat flux as a function of the damping constant g_m for (a) the forward and (b) the reverse scenarios (blue solid lines: evanescent p-polarization, green dashed lines: propagation p-polarization, pink dashed-double-dotted lines: evanescent s-polarization, red dashed-dotted lines: propagation s-polarization, black dotted lines: blackbody radiation). (For interpretation of the references to color in this figure legend, the reader is referred to the web version of this article.)

is as far away as possible from the bulk state resonance in the thermal excitation wavelengths.

4.2. Dependency of the contrast ratio on g_m

We next consider the effect of the damping constant g_m on thermal rectification. Fig. 6 shows the thermal rectification as a function of g_m. We see a maximum in the thermal rectification contrast ratio (blue solid line) of Fig. 6. In order to understand such behavior, in Fig. 6 we also plot S^0 and η that were defined in Eq. (5) as a function of g_m. As g_m decreases, we see that the rectification contrast ratio of the surface state increases. On the other hand, the contribution from the surface state to the total heat transfer, as characterized by η, decreases. These two competing trends result in the maximum-curve behavior of the contrast ratio as a function of g_m.

The amount of heat flux from metamaterials is strongly dependent on the damping constant g_m and is plotted as a function of g_m in Fig. 7(a) and (b). As g_m decreases, the surface state has a sharp resonance in each metamaterial plate and the contrast of heat flux arising from the alignment or misalignment of resonances is enhanced, which is seen as the increase of S^0 in Fig. 6. However, the amounts of heat flux for both scenarios are decreased for the surface state. On the other hand, the bulk state has almost a constant amount of heat flux when $g_m < 1 \times 10^{13}$ rad/s, which stems from the assumption of the semi-infinite plates. Therefore, the relative excitation of the surface state to the bulk state decreases, which is seen in Fig. 6 that η goes to zero, and thermal rectification is weakened. On the other hand, in the case of large g_m, the surface state resonance of each metamaterial plate becomes broadband with large heat flux that exceeds the heat flux of the bulk state excitation with $\eta \approx 1$. Such broadband thermal excitation reduces the spectral contrast S^0 between the forward and reverse scenarios for the surface state, resulting in the decrease of the rectification coefficient.

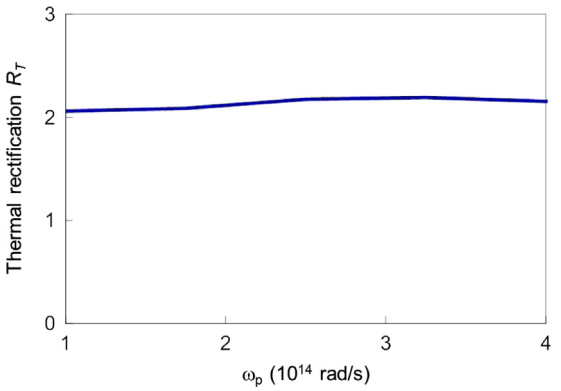

Fig. 8. Thermal rectification as a function of the plasma frequency ω_p in Eq. (1).

We have assumed a temperature-independent parameter of g_m for clear understanding of the operation mechanism in our thermal rectifier model. Thermal rectification is less sensitive to the temperature dependency of g_m. For example, a 20% variation of g_m between 300 K and 500 K with all other parameters in the caption of Fig. 1 being the same gives a 0.5% change in the contrast ratio of thermal rectification.

4.3. Dependency of the contrast ratio on ω_p

Thirdly, we examine the thermal rectification contrast ratio as a function of the plasma frequency ω_p (Fig. 8). The contrast ratio has a very weak dependency on ω_p. The contributions to the total heat flux from the surface and the bulk states both decrease with increase of ω_p. However, the contrast ratios of contributions of the surface state in the forward and reverse scenarios (S^0 in Eq. (5)) as well as the surface state and the bulk state (η in Eq. (5)) have very little dependency on ω_p, since both the surface resonance frequency and bulk resonance frequency shift

with the change of ω_p. As a result, the thermal rectification contrast ratio is weakly dependent on ω_p.

5. Conclusions

We have explored the relative excitation strength of the surface state and bulk state resonances in metamaterial based electromagnetic thermal rectifiers since the thermal rectification arises by the surface state contribution and the bulk state does not contribute to it. We have characterized the behavior of such thermal rectifiers by accounting for the dependence on the contrast ratio on various parameters that define the dielectric response of the metamaterials.

In electromagnetic thermal rectifiers, both the surface state and the bulk state are excited. Thus distinguishing different roles of the surface state and bulk state excitations is important. Previous studies on such thermal rectifiers have mainly discussed the contribution of the surface state excitation. By clarifying different roles of surface and bulk excitations, our results therefore point to an important physical understanding and design guideline for electromagnetic thermal rectifiers.

Acknowledgments

Prof. Fan's contribution to this publication was as a consultant, and was not part of his Stanford duties or responsibilities.

References

[1] Calhill DG, Braun PV, Chen G, Clarke DR, Fan S, Goodson KE, et al. Nanoscale thermal transport. II. 2003–2012. Appl Phys Rev 2014;1:011305–45.
[2] Polder D, Van Hove M. Theory of radiative heat transfer between closely spaced bodies. Phys Rev B 1971;4:3303–14.
[3] Pendry JB. Radiative exchange of heat between nanostructures. J Phys: Condens Matter 1999;11:6621–33.
[4] Fu CJ, Zhang ZM. Nanoscale radiation heat transfer for silicon at different doping levels. Int J Heat Mass Transfer 2006;49:1703–18.
[5] Basu S, Zhang ZM, Fu CJ. Review of near-field thermal radiation and its application to energy conversion. Int J Energy Res 2009;33:1203–32.
[6] Biehs SA, Greffet JJ. Near-field heat transfer between a nanoparticle and a rough surface. Phys Rev B 2010;81:245414-12.
[7] Otey C, Fan S. Numerically exact calculation of electromagnetic heat transfer between a dielectric sphere and plate. Phys Rev B 2011;84:245431–7.
[8] Kruger M, Emig T, Kardar M. Nonequilibrium electromagnetic fluctuations: heat transfer and interactions. Phys Rev Lett 2011;106:210404-4.
[9] Rodriguez AW, Ilic O, Bermel P, Celanovic I, Joannopoulos JD, Soljacic M, et al. Frequency-selective near-field radiative heat transfer between photonic crystal slabs: a computational approach for arbitrary geometries and materials. Phys Rev Lett 2011;107:114302–5.
[10] Biehs SA, Abdallah PB, Rosa FSS, Joulain K, Greffet JJ. Nanoscale heat flux between nanoporous materials. Opt Express 2011;19:A1088–103.
[11] Francoeur M, Menguc MP, Vaillon R. Coexistence of multiple regimes for near-field thermal radiation between two layers supporting surface phonon polaritons in the infrared. Phys Rev B 2011;84:075436–9.
[12] Messina R, Antezza M, Abdallah PB. Three-body amplification of photon heat tunneling. Phys Rev Lett 2012;109:244302.
[13] Otey CR, Zhu L, Sandhu S, Fan S. Fluctuational electrodynamics calculations of near-field heat transfer in non-planar geometries: a brief overview. J Quant Spec Radiat Trans 2014;132:3–11.
[14] Hu L, Narayanaswamy A, Chen X, Chen G. Near-field thermal radiation between two closely spaced glass plates exceeding Planck's blackbody radiation law. Appl Phys Lett 2008;92 (133106-3).
[15] Ottens RS, Questschke V, Wise S, Alemi AA, Lundock R, Mueller G, et al. Near-field radiative heat transfer between macroscopic planar surfaces. Phys Rev Lett 2011;107:014301–4.
[16] Kralik T, Hanzelka P, Zobac M, Musilova V, Fort T, Horak M. Strong near-field enhancement of radiative heat transfer between metallic surfaces. Phys Rev Lett 2012;109:224302–5.
[17] Shen S, Narayanaswamy A, Chen G. Surface phonon polaritons mediated energy transfer between nanoscale gaps. Nano Lett 2009;9:2909–13.
[18] Rousseau E, Siria A, Jourdan G, Volz S, Comin F, Chevrier J, et al. Radiative heat transfer at the nanoscale. Nat Photon 2009;3:514–7.
[19] Guha B, Otey C, Poitras CB, Fan S, Lipson M. Near-field radiative cooling of nanostructures. Nano Lett 2012;12:4546–50.
[20] Wilde YD, Formanek F, Carminati R, Gralak B, Lemoine PA, Joulain K, et al. Thermal radiation scanning tunnelling microscopy. Nature 2006;444:740–3.
[21] Wang L, Uppuluri SM, Jin EX, Xu X. Nanolithography using high transmission nanoscale bowtie apertures. Nano Lett 2006;6:361–4.
[22] Kittel A, Wischnath UF, Welker J, Huth O, Ruting F, Biehs SA. Near-field thermal imaging of nanostructured surfaces. Appl Phys Lett 2008;93:193109.
[23] Challener WA, Peng C, Itagi AV, Karns D, Peng W, Peng Y, et al. Heat-assisted magnetic recording by a near-field transducer with efficient optical energy transfer. Nat Photon 2009;3:220–4.
[24] Francoeur M, Vaillon R, Menguc MP. Thermal impacts on the performance of nanoscale-gap thermophotovoltaic power generators. IEEE Trans Energy Convers 2011;26:686–98.
[25] Jones AC, Raschke MB. Thermal infrared near-field spectroscopy. Nano Lett 2012;12:1475–81.
[26] Worbes L, Hellmann D, Kittel A. Enhanced near-field heat flow of a monolayer dielectric island. Phys Rev Lett 2013;110:134302.
[27] Joulain K, Drevillon J. Noncontact heat transfer between two metamaterials. Phys Rev B 2010;81 (165119-7).
[28] Francoeur M, Basu S, Petersen SJ. Electric and magnetic surface polaritons mediated near-field radiative heat transfer between metamaterials made of silicon carbide particles. Opt Express 2011;19:18774–88.
[29] Basu S, Francoeur M. Penetration depth in near-field radiative heat transfer between metamaterials. Appl Phys Lett 2011;99 (143107-3).
[30] Biehs SA, Tschikin M, Abdallah PB. Hyperbolic metamaterials as an analog of a blackbody in the near field. Phys Rev Lett 2012;109:104301–5.
[31] Petersen SJ, Basu S, Francoeur M. Near-field thermal emission from metamaterials. Phot Nano Fund Appl 2013;11:167–81.
[32] Cui L, Huang Y, Wang J, Zhu KY. Ultrafast modulation of near-field heat transfer with tunable metamaterials. Appl Phys Lett 2013;102 (053106-5).
[33] Otey CR, Lau WT, Fan S. Thermal rectification through vacuum. Phys Rev Lett 2010;104:154301–4.
[34] Iizuka H, Fan S. Rectification of evanescent heat transfer between dielectric-coated and uncoated silicon carbide plates. J Appl Phys 2012;112:024304–7.
[35] Wang LP, Zhang ZM. Thermal rectification enabled by near-field radiative heat transfer between intrinsic silicon and a dissimilar material. Nanosc Microscale Thermophys Eng 2013;17:337–48.
[36] Basu S, Francoeur M. Near-field radiative transfer based thermal rectification using doped silicon. Appl Phys Lett 2011;98 (113106-3).
[37] Yang Y, Basu S, Wang L. Radiation-based near-field thermal rectification with phase transition materials. Appl Phys Lett 2013;103:163101–5.
[38] Huang J, Li Q, Zheng Z, Xuan Y. Thermal rectification based on thermochromic materials. Int J Heat Mass Transfer 2013;67:575–80.
[39] Abdallah PB, Biehs SA. Phase-change radiative thermal diode. Appl Phys Lett 2013;103 (191907-3).
[40] Zhu L, Otey CR, Fan S. Ultrahigh-contrast and large-bandwidth thermal rectification in near-field electromagnetic thermal transfer between nanoparticles. Phys Rev B 2013;88:184301–8.
[41] Pendry JB, Holden AJ, Stewart WJ, Youngs I. Extremely low frequency plasmons in metallic mesostructures. Phys Rev Lett 1996;76:4773–6.
[42] Solymar L, Shamonina E. Waves in metamaterials. New York: Oxford University; 2009.

[43] Haus HA. Waves and fields in optoelectronics. Englewood Cliffs, NJ: Prentice-Hall; 1984.
[44] Biehs SA, Agarwal GS. Dynamical quantum theory of heat transfer between plasmonic nanosystems. J Opt Soc Am B 2013;30:700–7.
[45] Wang F, Shen YR. General properties of local plasmons in metal nanostructures. Phys Rev Lett 2006;97 (206806-4).
[46] Khurgin JB, Sun G. Scaling of losses with size and wavelength in nanoplasmonics and metamaterials. Appl Phys Lett 2011;99 (211106-3).
[47] Raman A, Shin W, Fan S. Upper bound on the modal material loss rate in plasmonic and metamaterial systems. Phys Rev Lett 2013;110:183901–5.